SEASONAL ANALYSIS OF ATTITUDE ESTIMATION ACCURACY FOR THE BRAZILIAN SATELLITE AMAZONIA-1 UNDER NORMAL AND FAULTY CONDITIONS

Ronan Arraes Jardim Chagas[(1)] **and Roberto Vieira da Fonseca Lopes**[(2)]

[(1)(2)]*Instituto Nacional de Pesquisas Espaciais, Av. Astronautas 1.758, Jd. da Granja, São José dos Campos, SP, Brazil*

[(1)]*+55-12-3208-7012, ronan.chagas@inpe.br*

[(2)]*+55-12-3208-7013, roberto.lopes@inpe.br*

Abstract: *The satellite Amazonia-1, which uses the Brazilian Multi-Mission Platform, has two star trackers and a four-axis fiber optic gyro to estimate the attitude at the routine operation mode. The gyro measurements are used to build the attitude estimation error model in which the state are estimated by means of a recursive filter. In a previous study, the attitude estimation error covariance was analyzed considering that both star trackers have constant accuracy. However, since the satellite will be placed on a sun-synchronous orbit pointing towards Earth, then each star tracker will have different set of stars in their field of view throughout the orbit. Thus, the measurement accuracy of these sensors will vary over the year. The star tracker manufacturer supplied a map that provides the sensor accuracy given the ascension and declination of its boresight axis represented in the J2000 reference frame. This new information is used to extend the aforementioned previous study to compute more realistically the statistics of the satellite attitude estimation errors. Moreover, this study analyzes the estimation accuracy under different scenarios of sensor failures.*

Keywords: *Attitude estimation, Star tracker, Fiber Optic Gyro, Kalman filter, MMP.*

1. Introduction

The Brazilian mission Amaziona-1 has as its primary objective the monitoring of the Amazonia rainforest. The satellite uses the Brazilian Multi-Mission Platform (MMP) and will be launch on a sun-synchronous, frozen orbit with semi-major axis of 7131.00 km, inclination of 98.405, eccentricity of 0.001111, and a RAAN such that the apparent local time at the illuminated part of the orbit is 10:30 AM [1].

The MMP uses two SED-26 star trackers and a four-axis fiber optic gyro Astrix-120 to estimate the attitude at the routine satellite operation mode (ROU). In this mode, the attitude determination process first evaluate a static estimate by combining the output quaternion from both star trackers and then the static estimate is filtered with the aid of the gyro measurements. The star trackers were positioned with their field of view orthogonal to each other in order to minimize the total error under the constraint that neither of them can point closer than a given excluding angle to the Sun nor to the Earth. In a previous study [2], the satellite attitude estimation accuracy was evaluated considering the star trackers with constant accuracy equivalent to their 3σ level over the whole celestial vault. However, the satellite will be Earth oriented on a sun-synchronous orbit and the star trackers will see different sets of stars throughout the orbit. In this scenario the measurement error statistics will vary, since the star trackers accuracy depends on the stars in their field of view [3].

The star tracker manufacturer, as can be seen in Fig. 1, provided data to obtain the low frequency

error (LFE) and 3σ noise equivalent error (NEA) as a function of the ascension and declination of the star tracker optical axis related to the J2000 coordinate frame. In this paper the aforementioned previous study is extended by using this novel information to compute more realistically the seasonal variation of the Amazonia-1 attitude estimation accuracy throughout the year. Moreover, this study provides additional information about the estimation accuracy under a set of possible failures.

The gyro measurements are used to build the attitude estimation error model in which the state can be estimated by means of a recursive filter. On the other hand, when the gyro measurements are not available, the attitude estimation is obtained by the static fusion of the both star trackers measurements. In this study, two filters were considered to fuse the gyro measurements. The first is the optimal Kalman filter that uses the true measurement covariance as provided by the manufacturer. The second is the constant gain filter that is the steady-state solution of the former based on a constant model of the star trackers accuracy. Notice that the latter is the algorithm embedded in the AOCS on-board computer.

In section 2, the coordinate frames used in this analysis are introduced. The mathematical modeling of the estimation and sensor errors can be seen in section 3. The results and analysis are presented in section 4 and, finally, the conclusions are in section 5.

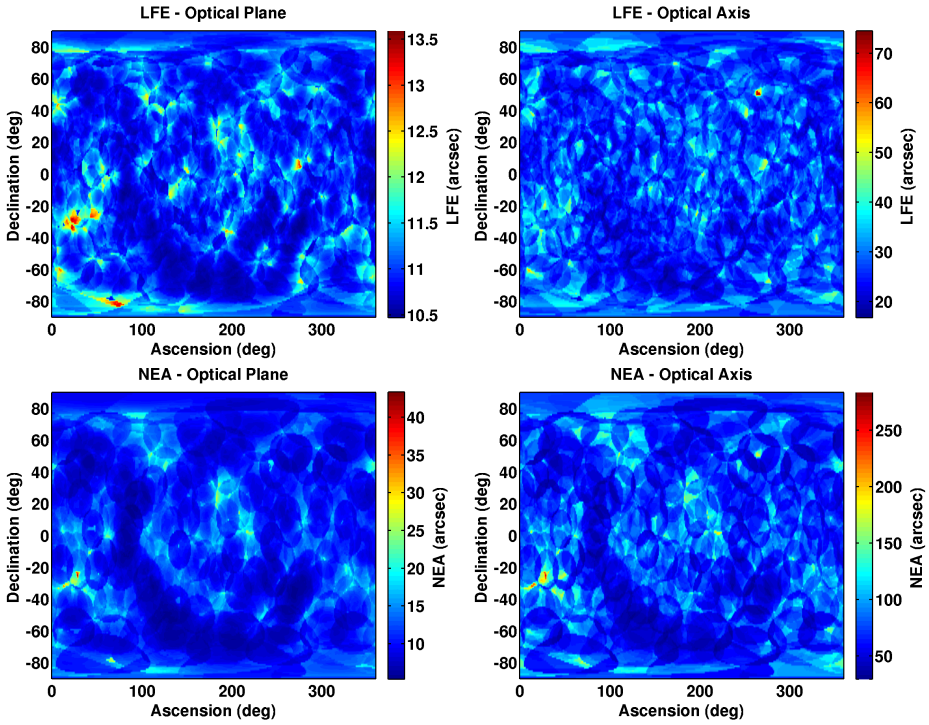

Figure 1. Low frequency error (LFE) and 3σ noise equivalent error (NEA) as a function of the ascension and declination of the star tracker optical axis in the J2000 coordinate frame. The left column contains the errors in the star tracker optical plane and the right column contains the errors in the star tracker optical axis.

2. Coordinate Frames

The coordinate frames used in this paper can be seen on Fig. 2. They are defined as follows:

- The inertial coordinate frame $\mathbf{S}_i$ is composed of the axes $\{\mathbf{x}_i,\ \mathbf{y}_i,\ \mathbf{z}_i\}$. Here it is defined as the J2000 coordinate system.
- The AOCS body coordinate frame $\mathbf{S}_b$ is composed of the axes $\{\mathbf{x}_b,\ \mathbf{y}_b,\ \mathbf{z}_b\}$ that are aligned with the satellite body as shown in Fig. 3. The estimation algorithm pursues to find the direction cosine matrix that rotates the inertial coordinate frame into alignment with the body coordinate frame.
- The computed coordinate frame $\mathbf{S}_c$ is composed of the axes $\{\mathbf{x}_c,\ \mathbf{y}_c,\ \mathbf{z}_c\}$ and is defined as the coordinate frame obtained by the on-board computer after fusing the available measurements from the FOG and the star trackers. Notice that if the measurements are ideal, then the body coordinate frame is equal to the computed coordinate frame.
- Each star tracker has its own coordinate frame in which its measurements are represented. It will be called $\mathbf{S}_{stra}$ for the star tracker A and $\mathbf{S}_{strb}$ for the star tracker B.

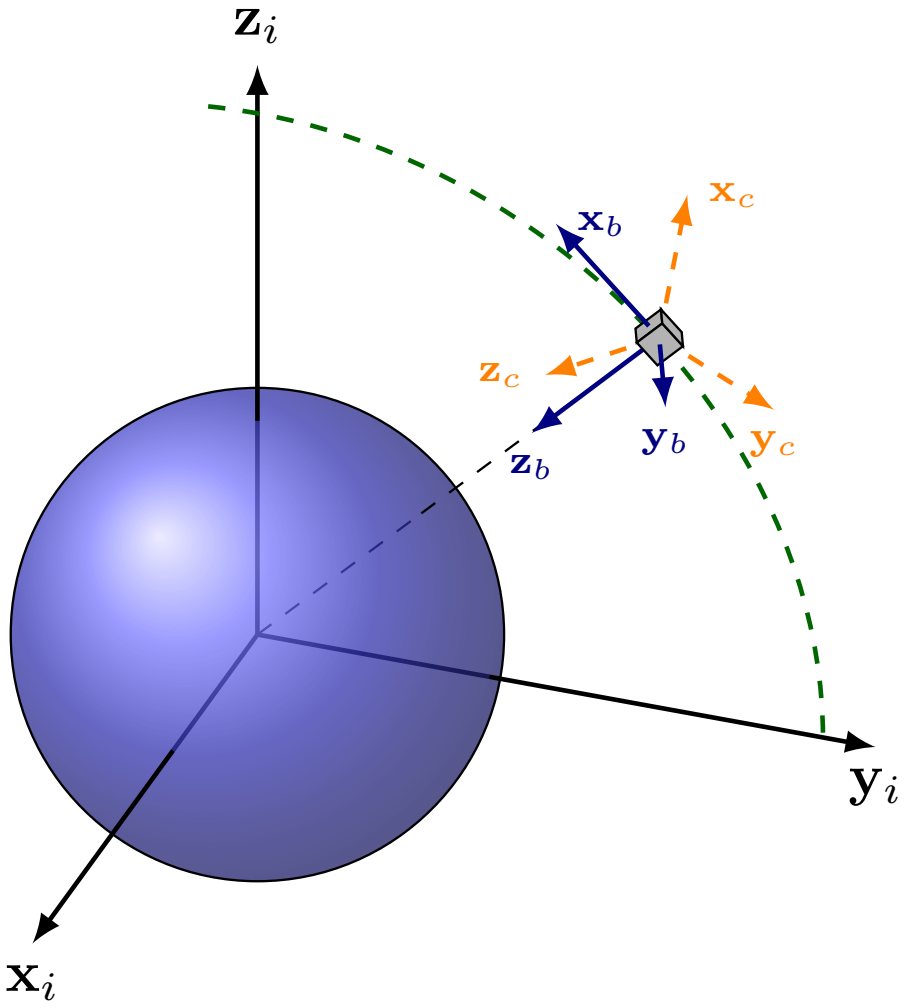

Figure 2. Coordinate frames.

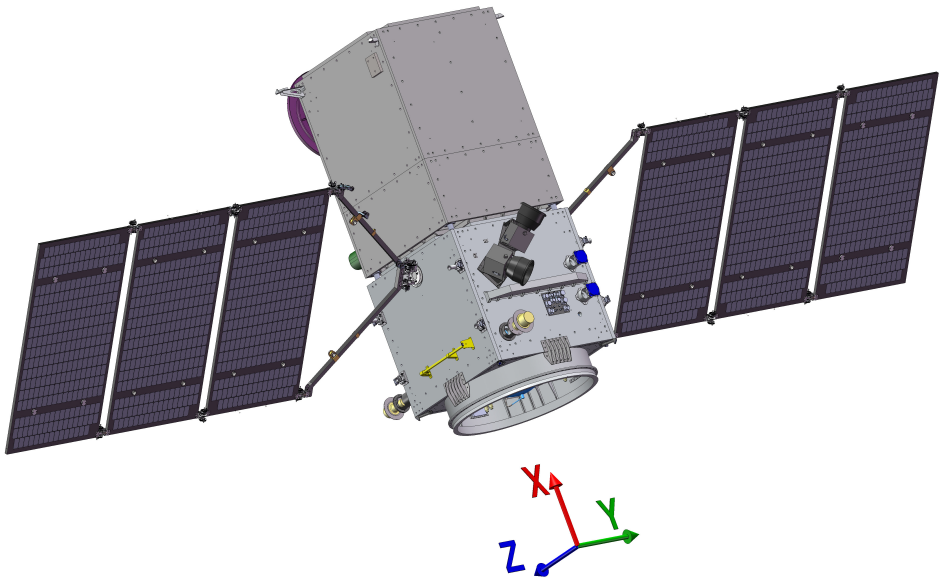

Figure 3. Body coordinate frame.

3. Mathematical Modeling

This section contains the mathematical modeling of the system. Since this paper pursues to quantify only the estimation errors, it is assumed that the control algorithm is ideal. Thus, the satellite angular velocity represented in the body coordinate frame is

$$\boldsymbol{\omega}_b = \begin{bmatrix} 0 & \Omega & 0 \end{bmatrix}^T \text{ rad/s}, \tag{1}$$

where Ω is the orbital angular velocity.

3.1. Fiber Optic Gyro Error Model

The FOG Astrix-120 has four channels arranged on a tetrahedron. Let g denote the FOG coordinate frame, then the error vector can be written as

$$\mathbf{e}_g = \mathbf{b}_g(t) + \mathbf{w}_{arw,g}(t) = \begin{bmatrix} b_1(t) \\ b_2(t) \\ b_3(t) \\ b_4(t) \end{bmatrix} + \begin{bmatrix} w_{arw,1}(t) \\ w_{arw,2}(t) \\ w_{arw,3}(t) \\ w_{arw,4}(t) \end{bmatrix}, \tag{2}$$

where $b_j(t)$ is the bias of j-th channel and $w_{arw,j}(t)$ is a white, Gaussian random process with power spectral density N_{arw} that is the source of the angular random walk about j-th axis, $j \in [1,2,3,4]$.

The direction cosines of FOG axes in the AOCS coordinate frame are

$$\mathbf{T}_g^b = \begin{pmatrix} \frac{1}{3} & -\frac{2\sqrt{2}}{3} & 0 \\ \frac{1}{3} & \frac{\sqrt{2}}{3} & -\frac{\sqrt{2}}{\sqrt{3}} \\ \frac{1}{3} & \frac{\sqrt{2}}{3} & \frac{\sqrt{2}}{\sqrt{3}} \\ -1 & 0 & 0 \end{pmatrix} \begin{matrix} \text{FOG 1} \\ \text{FOG 2} \\ \text{FOG 3} \\ \text{FOG 4} \end{matrix} . \tag{3}$$

Thus,

$$\begin{aligned} \boldsymbol{\omega}_g &= \mathbf{T}_g^b \boldsymbol{\omega}_b \\ \mathbf{T}_g^{b,T} \boldsymbol{\omega}_g &= \mathbf{T}_g^{b,T} \mathbf{T}_g^b \boldsymbol{\omega}_b \\ \underbrace{\left(\mathbf{T}_g^{b,T} \mathbf{T}_g^b\right)^{-1} \mathbf{T}_g^{b,T}}_{\mathbf{D}_b^g} \boldsymbol{\omega}_g &= \boldsymbol{\omega}_b \\ \mathbf{D}_b^g \boldsymbol{\omega}_g &= \boldsymbol{\omega}_b \ , \end{aligned} \tag{4}$$

where

$$\mathbf{D}_b^g = \begin{pmatrix} \frac{1}{4} & \frac{1}{4} & \frac{1}{4} & -\frac{3}{4} \\ -\frac{\sqrt{2}}{2} & \frac{\sqrt{2}}{4} & \frac{\sqrt{2}}{4} & 0 \\ 0 & -\frac{4}{3}\frac{\sqrt{2}}{\sqrt{3}} & \frac{4}{3}\frac{\sqrt{2}}{\sqrt{3}} & 0 \end{pmatrix} \tag{5}$$

is the matrix that represents the FOG measurements in the body coordinate frame. Notice that $\mathbf{D}_b^g$ **is not** a direction cosine matrix. Finally, the FOG error vector represented in the body coordinate frame can be written as

$$\begin{aligned} \mathbf{e}_b(t) &= \mathbf{D}_b^g \mathbf{e}_g(t) = \mathbf{D}_b^g \mathbf{b}_g(t) + \mathbf{D}_b^g \mathbf{w}_{arw,g}(t) \\ \mathbf{e}_b(t) &= \mathbf{b}_b(t) + \mathbf{D}_b^g \mathbf{w}_{arw,g}(t) \ . \end{aligned} \tag{6}$$

The bias continuous dynamic model about j-th FOG axis can be written as

$$\dot{b}_j(t) = -\lambda b_j(t) + v_j(t) \ , \tag{7}$$

where $\lambda \in \mathbb{R}$ and $v_j(t)$ is a white, Gaussian random process with power spectral density N_b. The solution of differential equation 7 is [4, 5]

$$b_j(t) = e^{-\lambda t} b_j(0) + \int_0^t e^{-\lambda(t-\tau)} v_j(\tau) d\tau \ . \tag{8}$$

Thus, the discrete solution can be written as

$$b_{j,k} = e^{-\lambda \Delta t} b_{j,k-1} + v_{j,k-1} \ , \tag{9}$$

where $b_{j,k} = b_j(t_k)$, $\Delta = t_k - t_{k-1}$, and $v_{j,k-1} = \int_0^{\Delta t} e^{-\lambda(\Delta t-\tau)} v_j(\tau + t_{k-1}) d\tau$.

It can be proved that $v_{j,k-1}$ is a Gaussian random variable [5]. Thus, it is only necessary to compute its mean and covariance [6]. Using the properties of expectation operator and that v_j is a white random process, one can see that [6]

$$E\{v_{j,k-1}\} = \int_0^{\Delta t} e^{-\lambda(\Delta t-\tau)} E\{v_j(\tau + t_{k-1})\} d\tau = 0 \ . \tag{10}$$

In the sequence, the covariance can be computed using

$$E\{v_{j,k-1}^2\} = E\left\{ \left(\int_0^{\Delta t} e^{-\lambda(\Delta t-\tau_1)} v_j(\tau_1 + t_{k-1}) d\tau_1 \right) . \left(\int_0^{\Delta t} e^{-\lambda(\Delta t-\tau_2)} v_j(\tau_2 + t_{k-1}) d\tau_2 \right) \right\} \tag{11}$$

that leads to

$$\begin{aligned} E\{v_{j,k-1}^2\} &= \int_0^{\Delta t} \int_0^{\Delta t} e^{-\lambda(t-\tau_1)} e^{-\lambda(t-\tau_2)} E\{v_j(\tau_1 + t_{k-1}) v_j(\tau_2 + t_{k-1})\} d\tau_1 d\tau_2 \\ E\{v_{j,k-1}^2\} &= \int_0^{\Delta t} \int_0^{\Delta t} e^{-\lambda(t-\tau_1)} e^{-\lambda(t-\tau_2)} N_b \delta(\tau_1 - \tau_2) d\tau_1 d\tau_2 \\ E\{v_{j,k-1}^2\} &= \frac{N_b}{2\lambda} \left(1 - e^{-2\lambda\Delta t} \right) = Q_b \left(1 - e^{-2\lambda\Delta t} \right) \ , \end{aligned} \tag{12}$$

where $\delta(t)$ is the Dirac delta and $Q_b = N_b/2\lambda$ is the gyro bias stability. The latter describes how the bias may change over a specified period of time $\tau = 1/\lambda$, typically around 100s, in fixed conditions [7]. Usually it is specified as a 1σ value with units $^\circ/h$ or $^\circ/s$.

The bias continuous model represented in the body coordinate frame can be written as

$$\dot{\mathbf{b}}_b(t) = \frac{d}{dt} \left(\mathbf{D}_b^g \mathbf{b}_g(t) \right) = \mathbf{D}_b^g \dot{\mathbf{b}}_g(t) = -\lambda \mathbf{D}_b^g \mathbf{b}_g(t) + \mathbf{D}_b^g \mathbf{v}_g(t) = -\lambda \mathbf{b}_b(t) + \mathbf{D}_b^g \mathbf{v}_g(t) \ , \tag{13}$$

where $\mathbf{v}_g(t) = \begin{bmatrix} v_1(t) & v_2(t) & v_3(t) & v_4(t) \end{bmatrix}^T$.

Finally, the FOG measurement represented in the body coordinate frame can be written as

$$\boldsymbol{\omega}_b^m = \boldsymbol{\omega}_b + \mathbf{e}_b \ , \tag{14}$$

where $\boldsymbol{\omega}_b$ is the true satellite body angular rate and $\mathbf{e}_b$ is the measurement error as in 6, both represented in the AOCS coordinate frame.

3.2. Dynamic Model of Attitude Determination Errors

Ideally, the on-board computer would compute the DCM $\mathbf{D}_i^b$ that rotates the body coordinate frame onto the inertial coordinate frame. This matrix can be computed by integrating the differential equation [8]

$$\dot{\mathbf{D}}_i^b = \mathbf{D}_i^b \left[\boldsymbol{\omega}_b \right]_\times \ , \tag{15}$$

where $[\mathbf{v}]_\times$ is the skew-symmetric matrix that represents the cross product. However, since the true angular velocity $\boldsymbol{\omega}_b$ is not available, the on-board computer will use the FOG measurement in 14 to compute to following DCM:

$$\dot{\mathbf{D}}_i^c = \mathbf{D}_i^c \left[\boldsymbol{\omega}_b^m\right]_\times \ . \tag{16}$$

Notice that the computed coordinate frame and the body coordinate frame are misaligned due to the FOG measurement errors only. It is assumed that such errors are small enough to yield small misalignment angles between these two coordinate frames. Thus, it can be written that [8]

$$\mathbf{D}_b^c \approx \mathbf{I}_3 + \left[\Delta\boldsymbol{\theta}\right]_\times \ , \tag{17}$$

where $\Delta\boldsymbol{\theta} = \begin{bmatrix}\theta_{a,x} & \theta_{a,y} & \theta_{a,z}\end{bmatrix}$ is a vector composed of the misalignment angles about the body axes.

Using 14 in 16 and neglecting second order terms, it can be proved that

$$\left[\dot{\Delta\boldsymbol{\theta}}\right]_\times = \left[\Delta\boldsymbol{\theta}\right]_\times \left[\boldsymbol{\omega}_b\right]_\times - \left[\boldsymbol{\omega}_b\right]_\times \left[\Delta\boldsymbol{\theta}\right]_\times + \left[\mathbf{e}_b\right]_\times \ . \tag{18}$$

Additionally, one can see that

$$\left[\Delta\boldsymbol{\theta}\right]_\times \left[\boldsymbol{\omega}_b\right]_\times - \left[\boldsymbol{\omega}_b\right]_\times \left[\Delta\boldsymbol{\theta}\right]_\times = \left[\boldsymbol{\omega}_b \times \Delta\boldsymbol{\theta}\right]_\times = \left[\left[\boldsymbol{\omega}_b\right]_\times \Delta\boldsymbol{\theta}\right]_\times \ . \tag{19}$$

Finally the continuous dynamic model of the misalignment angles can be written as

$$\dot{\Delta\boldsymbol{\theta}} = \left[\boldsymbol{\omega}_b\right]_\times \Delta\boldsymbol{\theta} + \mathbf{e}_b \ , \tag{20}$$

where $\boldsymbol{\omega}_b$ is given by 1.

The state-vector used in this analysis is composed of the misalignment angles and the FOG bias. Thus, using 6, 13, and 20, the continuous dynamic model can be written as

$$\begin{bmatrix}\dot{\Delta\boldsymbol{\theta}} \\ \dot{\mathbf{b}}_b\end{bmatrix} = \begin{bmatrix}\left[\boldsymbol{\omega}_b\right]_\times & \mathbf{I}_3 \\ \mathbf{0}_{3\times3} & -\lambda\mathbf{I}_3\end{bmatrix} \begin{bmatrix}\Delta\boldsymbol{\theta} \\ \mathbf{b}_b\end{bmatrix} + \begin{bmatrix}\mathbf{D}_b^g \mathbf{w}_{arw,g} \\ \mathbf{D}_b^g \mathbf{v}_g\end{bmatrix} \ . \tag{21}$$

Let Δt be the gyro sampling interval, then, using the linear system theory and the result in 12, it can be proved that discretization of the continuous linear system in 21 leads to

$$\mathbf{x}_k = \mathbf{F}\mathbf{x}_{k-1} + \mathbf{w}_{k-1} \ , \tag{22}$$

where

$$\mathbf{F} = \left[\begin{array}{ccc|ccc} \cos(\Omega\Delta t) & 0 & -\sin(\Omega\Delta t) & \beta_1(\Delta t) & 0 & -\beta_2(\Delta t) \\ 0 & 1 & 0 & 0 & \beta_3(\Delta t) & 0 \\ \sin(\Omega\Delta t) & 0 & \cos(\Omega\Delta t) & \beta_2(\Delta t) & 0 & \beta_1(\Delta t) \\ \hline 0 & 0 & 0 & e^{-\lambda\Delta t} & 0 & 0 \\ 0 & 0 & 0 & 0 & e^{-\lambda\Delta t} & 0 \\ 0 & 0 & 0 & 0 & 0 & e^{-\lambda\Delta t} \end{array}\right] \ , \tag{23}$$

$$\beta_1(\Delta t) = \frac{\lambda}{\lambda^2+\Omega^2}\cos(\Omega\Delta t) + \frac{\Omega}{\lambda^2+\Omega^2}\sin(\Omega\Delta t) - \frac{\lambda}{\lambda^2+\Omega^2}e^{-\lambda\Delta t} ,$$
$$\beta_2(\Delta t) = \frac{\lambda}{\lambda^2+\Omega^2}\sin(\Omega\Delta t) - \frac{\Omega}{\lambda^2+\Omega^2}\cos(\Omega\Delta t) + \frac{\Omega}{\lambda^2+\Omega^2}e^{-\lambda\Delta t} ,$$
$$\beta_3(\Delta t) = \frac{1}{\lambda}\left(1-e^{-\lambda\Delta t}\right) ,$$

and $\mathbf{w}_{k-1}$ is a Gaussian random variable with zero mean and covariance matrix

$$\mathbf{Q} = \frac{3}{4}\cdot\left[\begin{array}{ccc|ccc} q_1(\Delta t) & 0 & 0 & q_3(\Delta t) & 0 & -q_4(\Delta t) \\ 0 & q_2(\Delta t) & 0 & 0 & q_5(\Delta t) & 0 \\ 0 & 0 & q_1(\Delta t) & q_4(\Delta t) & 0 & q_3(\Delta t) \\ \hline q_3(\Delta t) & 0 & q_4(\Delta t) & Q_b(1-e^{-2\lambda\Delta t}) & 0 & 0 \\ 0 & q_5(\Delta t) & 0 & 0 & Q_b(1-e^{-2\lambda\Delta t}) & 0 \\ -q_4(\Delta t) & 0 & q_3(\Delta t) & 0 & 0 & Q_b(1-e^{-2\lambda\Delta t}) \end{array}\right] , \tag{24}$$

$$q_1(\Delta t) = N_{arw}\Delta t + \frac{2Q_b\lambda}{\lambda^2+\Omega^2}\cdot\left[\Delta t - \frac{2\lambda}{\lambda^2+\Omega^2}\left(1-e^{-\lambda\Delta t}\cos(\Omega\Delta t)\right) + \frac{2\Omega}{\lambda^2+\Omega^2}e^{-\lambda\Delta t}\sin(\Omega\Delta t) + \frac{1}{2\lambda}\left(1-e^{-2\lambda\Delta t}\right)\right] ,$$
$$q_2(\Delta t) = N_{arw}\Delta t + \frac{2Q_b}{\lambda}\left[\Delta t - \frac{2}{\lambda}\left(1-e^{-\lambda\Delta t}\right) + \frac{1}{2\lambda}\left(1-e^{-2\lambda\Delta t}\right)\right] ,$$
$$q_3(\Delta t) = \frac{Q_b\lambda}{\lambda^2+\Omega^2}\left[1+e^{-2\lambda\Delta t} - 2e^{-\lambda\Delta t}\cos(\Omega\Delta t)\right] ,$$
$$q_4(\Delta t) = \frac{Q_b}{\lambda^2+\Omega^2}\left[\Omega(1-e^{-2\lambda\Delta t}) - 2\lambda e^{-\lambda\Delta t}\sin(\Omega\Delta t)\right] ,$$
$$q_5(\Delta t) = \frac{Q_b}{\lambda}\left[1-2e^{-\lambda\Delta t}+e^{-2\lambda\Delta t}\right] .$$

Notice that the gain $3/4$ in the covariance matrix is the result of using the 4-channels of the gyro to estimate the angular velocity about the three body axes.

3.3. Star Tracker Error Model

The attitude determination by a star tracker is based on the image centroid of several stars in the sensor field of view. The resulting accuracy is a function of accuracy of each star position measurement and the geometric pattern of the observed stars, which are dependent of the sky region observed by the sensor. Additionally, due to the sensor limited field of view, accuracy is several times better about the focal plane axes than about the sensor boresight axis [3]. Furthermore, the accuracy is usually limited by three different types of errors: Noise Equivalent Angle (NEA); Low Frequency Error (LFE); and Bias, as described in the sequence [3].

NEA is mainly due to optic and electronic noises, the first one caused by incident radiation from sky darkness background and the second is intrinsic from electronic components [3]. The standard variation of the NEA about each sensor axis is given by the sensor manufacturer as a function of sensor boresight direction over the celestial vault, as can be seen in Fig. 1.

LFE is mainly due to several aberration effects on non-ideal sensor optics and thermo elastic effects. For a given sensor attitude with respect to the stars and a given sensor temperature such error remains basically the same. Nevertheless, as the scenario changes with time due to spacecraft orbital motion, LFE experiments slow variations. Such effects can be mitigated by factory calibration. However, since optic distortions are a function of light spectrum and position of each star in the sensor field of view, and this function changes with sensor temperature, residual calibration errors are practically unavoidable as they experiment a too large number of degrees of freedom to be fully reproduced in laboratory [9]. An upper limit to the LFE after calibration is evaluated by the sensor manufacturer as a function of the sensor boresight direction on the celestial vault, as can be seen in Fig. 1.

Finally, bias is a constant but unknown error due to both internal and external misalignments after launch mainly caused by launching vibrations as well as to zero-g effects [9].

Boresight accuracy deficiency can be mitigated by data fusion of two star trackers placed one orthogonal to each other [2]. This has also a benefic effect on NEA about any axis. As for the accuracy level variations over the celestial vault, it is usually better than average when bright stars are observed, while sky regions with low star density are likely to present a poor accuracy [3]. Such accuracy irregular pattern can be smoothed by data filtering feed by gyro measurements. Finally, for remote sensing missions, bias can be mitigated by after launch ground calibration aided by landmarks, hence this component of the star tracker measurement error has been neglected in this analysis.

For simulation purposes, NEA is modeled as a random Gaussian white sequence with given covariance matrix for each direction of the sensor boresight. Due to the random nature of NEA sources, it is considered a spatially uncorrelated error, therefore with diagonal covariance matrix when represented in the i-th star tracker coordinate frame:

$$\mathbf{R}_{stri,k}^{stri} = \begin{pmatrix} \sigma_{xy}^2(\mathbf{u}_{stri,k}) & 0 & 0 \\ 0 & \sigma_{xy}^2(\mathbf{u}_{stri,k}) & 0 \\ 0 & 0 & \sigma_z^2(\mathbf{u}_{stri,k}) \end{pmatrix} , \tag{25}$$

where σ_{xy} and σ_z are the NEA standard deviation about the focal plane axes and the boresight axis respectively, and $\mathbf{u}_{stri,k}$ is the unit vector in the sensor boresight direction of the i-th star tracker at instant k.

In this work, LFE was simulated as the worst case among the eight possibilities with maximum absolute value in each axis:

$$\boldsymbol{\varepsilon}_{stri,k} = \begin{pmatrix} \Delta_{xy}(\mathbf{u}_{stri,k}) \\ \Delta_{xy}(\mathbf{u}_{stri,k}) \\ \Delta_z(\mathbf{u}_{stri,k}) \end{pmatrix} , \tag{26}$$

where Δ_{xy} and Δ_z are the LFE upper limit about the focal plane axes and the boresight axis respectively. Worst case among the eight possible signal combinations means the one with worst effect after data fusion of both star trackers. However this approach, besides requiring checking 64 signal combinations, is too conservative since it would require worst conditions on sensor

temperature and position of each star in the field of view of both sensors in every sensor axis simultaneously. Future work will focus on a more realistic LFE representation.

Finally, considering the dynamic model in 22, the i-th star tracker measurement at instant k represented in the body coordinate frame can be written as

$$\mathbf{y}_{b,k}^{stri} = \begin{bmatrix} 1 & 0 & 0 & 0 & 0 & 0 \\ 0 & 1 & 0 & 0 & 0 & 0 \\ 0 & 0 & 1 & 0 & 0 & 0 \end{bmatrix} \mathbf{x}_k + \mathbf{D}_b^{stri} \boldsymbol{\varepsilon}_{stri,k} + \mathbf{D}_b^{stri} \mathbf{v}_{stri,k} \ , \tag{27}$$

where $\mathbf{v}_{stri,k}$ is a Gaussian random variable with zero mean and $\mathbf{R}_{stri,k}^{stri}$ covariance. If the measurements of both star trackers are available, they can be fused using [6]

$$\begin{aligned} \mathbf{y}_{b,k}^{f} &= \left(\mathbf{R}_{b,k}^{stra,-1} + \mathbf{R}_{b,k}^{strb,-1} \right)^{-1} \left(\mathbf{R}_{b,k}^{stra,-1} \mathbf{y}_{b,k}^{stra} + \mathbf{R}_{b,k}^{strb,-1} \mathbf{y}_{b,k}^{strb} \right) \ , \\ \mathbf{y}_{b,k}^{f} &= \begin{bmatrix} 1 & 0 & 0 & 0 & 0 & 0 \\ 0 & 1 & 0 & 0 & 0 & 0 \\ 0 & 0 & 1 & 0 & 0 & 0 \end{bmatrix} \mathbf{x}_k + \boldsymbol{\varepsilon}_k^f + \mathbf{v}_k^f \ , \\ \boldsymbol{\varepsilon}_k^f &= \left(\mathbf{R}_{b,k}^{stra,-1} + \mathbf{R}_{b,k}^{strb,-1} \right)^{-1} \left(\mathbf{R}_{b,k}^{stra,-1} \mathbf{D}_b^{stra} \boldsymbol{\varepsilon}_{stra,k} + \mathbf{R}_{b,k}^{strb,-1} \mathbf{D}_b^{strb} \boldsymbol{\varepsilon}_{strb,k} \right) \ , \\ \mathbf{v}_k^f &= \left(\mathbf{R}_{b,k}^{stra,-1} + \mathbf{R}_{b,k}^{strb,-1} \right)^{-1} \left(\mathbf{R}_{b,k}^{stra,-1} \mathbf{D}_b^{stra} \mathbf{v}_{stra,k} + \mathbf{R}_{b,k}^{strb,-1} \mathbf{D}_b^{strb} \mathbf{v}_{strb,k} \right) \ , \end{aligned} \tag{28}$$

where $\mathbf{R}_{b,k}^{stri}$ is the covariance of the i-th star tracker represented in the body coordinate frame.

4. Results and Analysis

The attitude estimation accuracy for this study has been obtained by simulating the satellite orbit and attitude to compute the vectors represented in the J2000 coordinate frame that are aligned with the star tracker optical axes ($\mathbf{u}_{stra,k}$ and $\mathbf{u}_{strb,k}$). Then, using the information from the manufacturer in Fig. 1, it has been possible to compute the LFE and NEA for each sensor. These errors have been evaluated for each satellite position at each orbital plane during one year and the attitude estimation accuracy has been obtained for several scenarios regarding the considered set of attitude sensors. First the analysis has considered the routine operation mode, when all the sensors are fully available. Then the analysis is repeated for different sensor failure scenarios as indicated in Tab. 1.

In scenarios 01 to 06, the star tracker measurements were fused by means of a recursive filter in which the dynamic model is constructed using 22 and 27. In scenarios 01, 03, and 05, the filtering algorithm is the Kalman filter using the true measurement error covariance of the star trackers as provided by the manufacturer. However, such information is not embedded in the AOCS on-board computer. Therefore, it uses a constant gain filter algorithm that is the steady-state solution of the Kalman filter [10] based on the constant model of the star trackers accuracy. This algorithm was used in scenarios 02, 04, and 06. In scenarios 07 and 08, the measurements of both star trackers were represented in a common coordinate frame and then were fused using a static algorithm to minimize the fused measurement noise covariance. The scenario 07 used the true covariance (NEA) as provided by the manufacturer whereas the scenario 08 used the average over the whole celestial

Table 1. Scenarios.

Scenario	Available Sensors			Fusion Algorithm
	Star Tracker A	Star Tracker B	FOG	
01	X	X	X	Kalman filter
02	X	X	X	Constant gain filter
03	X		X	Kalman filter
04	X		X	Constant gain filter
05		X	X	Kalman filter
06		X	X	Constant gain filter
07	X	X		Inverse covariance (true)
08	X	X		Inverse covariance (mean value)
09	X			None
10		X		None

Table 2. Simulation parameters.

Parameter	Description	Value	Unit
Δt	FOG sampling step.	0.01	s
$\sqrt{N_{arw}}$	FOG angular random walk.	0.00101	$\circ/\sqrt{\text{h}}$
$\sqrt{Q_b}$	Bias stability of the FOG.	0.0008	arcsec
λ	Bias model time constant.	0.01	$1/\text{s}$
$\sigma_{xy,m}$	NEA mean value over the celestial vault for both star trackers in the **optical plane** for scenarios 02, 04, 06, and 08.	0.0035	arcsec
$\sigma_{z,m}$	NEA mean value over the celestial vault for both star trackers in the **optical axis** for scenarios 02, 04, 06, and 08.	0.02	arcsec

vault, as embedded in the AOCS on-board computer. Some simulation parameters can be found on Tab. 2.

The purpose to compare the optimal Kalman filter (scenarios 01, 03, and 05) to the filter embedded in the on-board computer (scenarios 02, 04, and 06) is to quantify if the degradation of the attitude estimation accuracy due to the use of a suboptimal algorithm is noticeable. The other scenarios were proposed to evaluate the attitude estimation accuracy degradation under a set of possible sensor failures.

The attitude estimation accuracy can be measured by two components: 1) one low frequency error (LFE) that is the result of the Star Tracker LFE and the gyro bias; and 2) one high frequency error (NEA) that is the result of the sensor noises. These errors were computed for each satellite position through one entire year and the statistics of these groups for each scenario can be seen in Tab. 3. Notice that the total error is obtained by summing LFE with 3σ NEA for each sampling interval. Additionally, in Fig. 4, the error maps computed for the scenario 02, which simulates the satellite routine operation mode, are plotted. These maps show the computed attitude estimation accuracy in

terms of LFE, NEA, and the total error for each satellite position (true anomaly) vs. all the orbital planes in one entire year. Notice that only the illuminated part of the orbit was considered for this analysis, since the Amazonia-1 payload is optic. The maps for the other scenarios have been omitted for the sake of compactness.

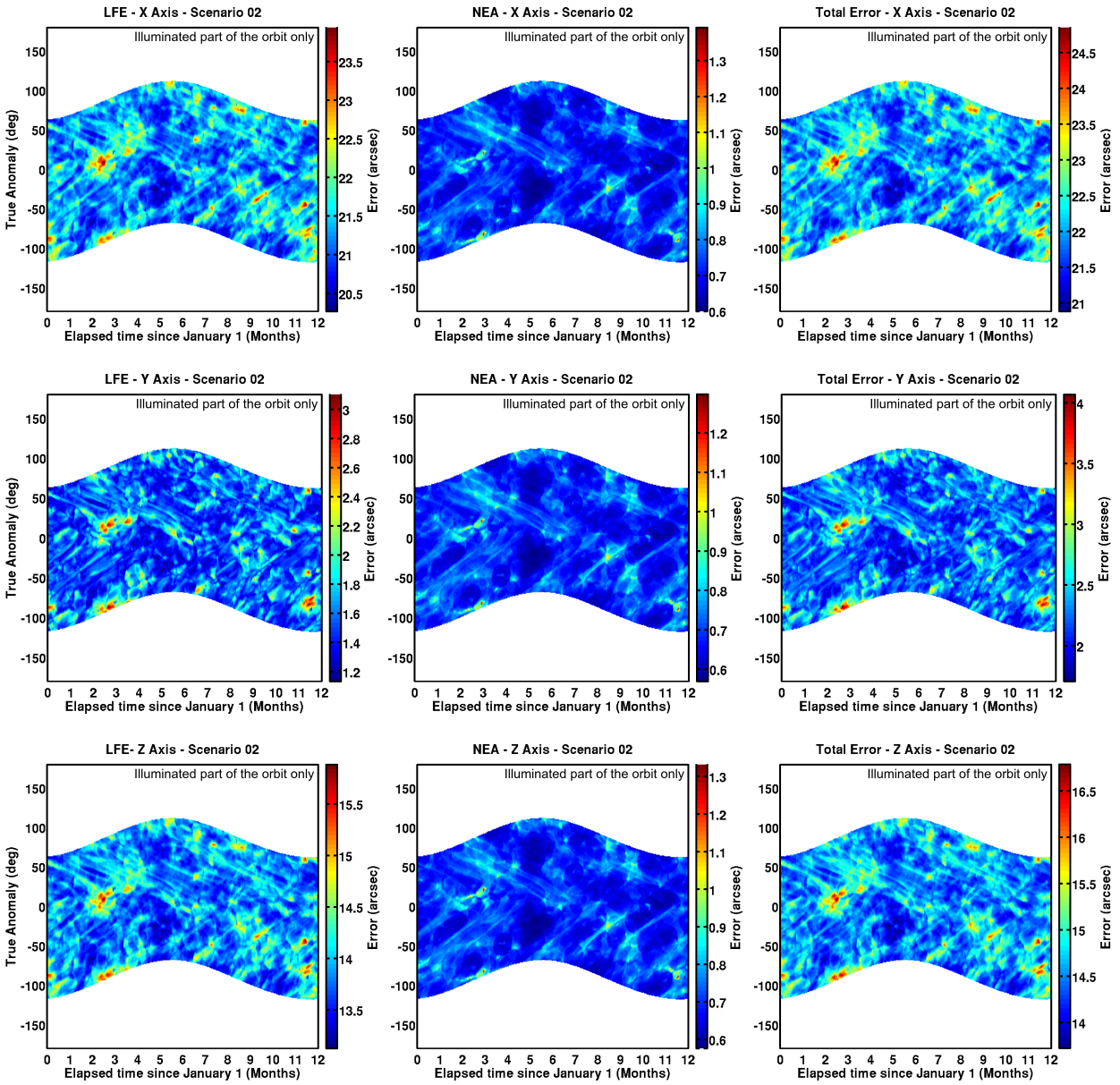

Figure 4. Computed errors for the scenario 02. The X, Y, and Z axes are shown in the first, second, and third rows respectively.

The results in Tab. 3 and in Fig. 4 lead to the following conclusions:

- The filter using the FOG (scenarios 01 to 06) greatly reduces the NEA, but the LFE is almost the same when comparing to the scenarios in which the estimate is carried out by a static algorithm, when the gyro is not available (scenarios 07 to 10).
- The Kalman filter (scenarios 01, 03, and 05) and the static fusion using the true inverse covariance (scenario 07) are optimal algorithms in terms of minimization of error covariance.

Table 3. Percentiles of the computed errors for each scenario.

		LFE (arcsec)			3σ **NEA** (arcsec)			**Total** (arcsec)		
Scenario	**Axis**	**0%**	**50%**	**98%**	**0%**	**50%**	**98%**	**0%**	**50%**	**98%**
	X	20.17	21.22	22.36	0.52	0.70	0.84	20.75	21.92	23.15
1	**Y**	0.62	3.74	9.15	0.49	0.66	0.79	1.24	4.40	9.84
	Z	12.97	14.74	16.94	0.50	0.67	0.81	13.49	15.41	17.66
	X	20.27	21.28	22.49	0.60	0.72	0.88	20.88	22.00	23.30
2	**Y**	1.13	1.54	2.21	0.57	0.68	0.84	1.70	2.23	2.94
	Z	13.13	13.84	14.74	0.58	0.69	0.85	13.72	14.54	15.51
	X	22.87	27.83	31.83	0.92	1.32	1.66	23.89	29.17	33.27
3	**Y**	21.38	25.60	28.97	0.78	1.11	1.40	22.20	26.72	30.21
	Z	19.84	24.86	28.65	0.84	1.19	1.48	20.72	26.07	29.99
	X	23.04	28.19	33.02	1.09	1.34	1.82	24.17	29.56	34.65
4	**Y**	21.76	25.86	29.76	0.93	1.13	1.51	22.73	27.02	31.12
	Z	20.76	25.13	29.24	1.00	1.21	1.61	21.79	26.36	30.68
	X	23.84	29.78	35.30	0.97	1.39	1.72	24.87	31.19	36.89
5	**Y**	21.08	25.41	29.58	0.78	1.12	1.40	21.92	26.55	30.90
	Z	18.33	22.32	26.21	0.79	1.14	1.43	19.18	23.47	27.52
	X	24.76	30.03	35.89	1.14	1.42	1.92	25.93	31.49	37.64
6	**Y**	21.63	25.61	30.10	0.92	1.14	1.54	22.58	26.78	31.53
	Z	18.61	22.59	27.00	0.93	1.16	1.57	19.57	23.78	28.44
	X	20.17	21.21	22.50	5.43	10.11	14.95	25.64	31.40	36.98
7	**Y**	0.65	3.79	9.40	4.97	9.10	13.30	6.12	13.10	20.64
	Z	12.98	14.76	17.14	5.07	9.36	13.74	18.18	24.29	29.84
	X	20.20	21.27	22.57	5.44	10.22	15.28	25.70	31.56	37.26
8	**Y**	1.16	1.58	2.31	4.98	9.39	14.08	6.20	11.04	15.88
	Z	13.09	13.86	14.89	5.08	9.62	14.43	18.20	23.56	28.81
	X	22.24	29.00	37.06	19.59	44.88	84.08	43.04	74.53	118.00
9	**Y**	20.60	26.03	32.50	15.67	35.61	66.58	37.23	62.15	96.65
	Z	18.41	24.34	31.44	17.58	40.13	75.16	37.05	65.07	103.81
	X	22.42	29.23	38.13	21.27	49.32	91.42	45.00	79.24	126.63
10	**Y**	20.19	25.24	31.85	15.63	35.96	66.35	36.78	61.71	96.11
	Z	17.64	22.55	28.96	15.55	35.77	65.99	34.13	58.82	92.87

Thus, as it can be seen, the NEA are always smaller than that of the scenarios using suboptimal algorithms. However, this is not true for the LFE. For example, the suboptimal algorithm in scenario 02 outweighs the performance of the optimal one in scenario 01 for the Y axis. In this case, the constant gain matrix of the suboptimal algorithm combines the star trackers measurements in such a way that the fused LFE is much smaller than that obtained by the optimal Kalman filter gain. Therefore, since the LFE value is much bigger than the NEA, the total computed error for this case is smaller for the suboptimal filter.

- The effect of locally poor accuracy areas over the celestial vault, Fig. 1, is mitigated by the combination of the two star trackers together with the filtering process using the gyro measurements.

5. Conclusions

This novel analysis extended the previous study about the Amazonia-1 estimation accuracy by adding a more realistic error model of the star tracker measurements that takes into account the satellite orbit and attitude. Moreover, it provided additional information about the mission performance under a set of possible sensor failures. Ten different scenarios were proposed considering distinct sets of sensors. When the gyro measurements are available, it is possible to construct the attitude error dynamic model and estimate the state using a recursive filter. In this analysis, two filters were evaluated: the Kalman filter and the constant gain filter, which is the filter embedded on the on-board computer and is obtained from the Kalman filter steady-state response.

It was verified that in the routine operation mode the effect of taking into account the star tracker accuracy variation on the filter gain evaluation was not benefic comparing to the constant accuracy model due to the presence of low frequency errors (LFE). Also, effect of locally poor accuracy areas over the celestial vault were mitigated by the combination of two star trackers and remarkably smoothed by the filtering process with the gyro. The same does not happen under some sensor failure conditions, when the current analysis becomes a more realistic accuracy prediction tool.

The filtering process helped to reduce the high frequency errors (NEA). Since the Kalman filter was designed to provide the minimum mean square error estimate, the NEA obtained in these scenarios was smaller than that of the scenarios using the constant gain filter. However, the magnitude of the low frequency errors (LFE) when both star trackers measurements are available is much bigger than that of NEA. Thus, it was verified that in some cases the total error using the constant gain filter was smaller than that of the Kalman filter because of how the former combines the measurements using the constant gain matrix.

Notice that if both star trackers have the same accuracy over the whole celestial vault, then the fused measurement error is minimized by positioning the sensors with their optical axes orthogonal to each other. However, the star tracker accuracy depends on the set of stars in its field of view. Thus, further study will focus on how the two sensors can be positioned to minimize the total estimation error.

Acknowledgments

The first author acknowledges the INPE researcher Mr. Márcio Afonso Arimura Fialho for the technical communications, Mr. Lincoln Azevedo for the Amazonia-1 figure presented here, and the Instituto Nacional de Ciência e Tecnologia (INCT) de Estudo do Espaço and the project FINEP/DCTA/INPE Sistemas Inerciais para Aplicação Aeroespacial (SIA) for the financial support.

6. References

[1] Lopes, R. V. F., Silva, A. R., Relloso, J., and Jun, Y. “Analysis of Albedo Effects on Coarse Sun Direction Determination Algorithms.” Proceedings of the 22nd International Symposium on Space Flight Dynamics — 22nd ISSFD. São José dos Campos, SP, Brazil, 2011.

[2] Lopes, R. V. F. "Star Tracker - Mechanical Configuration & Pointing Accuracy Analysis." Tech. Rep. 0858-CASV-0ICGU-001-A, INPE & INVAP, October 2010.

[3] Liebe, C. C. "Accuracy Performance of Star Trackers - A Tutorial." IEEE Transactions on Aerospace and Electronic Systems, Vol. 38, No. 2, pp. 587–599, 2002.

[4] Chen, C.-T. Linear System Theory and Design. CBS College Publishing, New York, NY, USA, 1984.

[5] Kloeden, P. E. and Platen, E. Numerical Solution of Stochastic Differential Equations. Springer, Berlin, Germany, 1999.

[6] Papoulis, A. and Pillai, S. U. Probability, Random Variables and Stochastic Processes. Mcgraw-Hill Companies, Inc., New York, NY, USA, 2002.

[7] Woodman, O. J. "An Introduction to Inertial Navigation." Tech. Rep. UCAM-CL-TR-696, Computer Laboratory, University of Cambridge, Cambridge, United Kingdom, August 2007.

[8] Sidi, M. J. Spacecraft Dynamics & Control: A Practical Engineering Approach. Cambridge University Press, New York, NY, USA, 1997.

[9] Lopes, R. V. F. and Shuster, M. D. "Parameter Interference in Distortion and Alignment Calibration." The Journal of the Astronautical Sciences, Vol. 51, No. 3, pp. 261–277, 2003.

[10] Anderson, B. D. O. and Moore, J. B. Optimal Filtering. Prentice-Hall, Inc., Englewood Cliffs, NJ, USA, 1979.